11th World Congress on Computational Mechanics (WCCM XI)
5th European Conference on Computational Mechanics (ECCM V)
6th European Conference on Computational Fluid Dynamics (ECFD VI)
Ryosuke Hayashi and Makoto Yamamoto (Eds)

ICING SIMULATION ON JET ENGINE WITH TEMPERATURE CHANGE OF SUPER-COOLED DROPLET

RYOSUKE HAYASHI[*], MAKOTO YAMAMOTO[†]

[*] Graduate School of Mechanical Engineering, Tokyo University of Science
6-3-1 Niijuku, Katsushika-ku, Tokyo, Japan
e-mail: j4512703@ed.tus.ac.jp

[†]Department of Mechanical Engineering, Tokyo University of Science
6-3-1 Niijuku, Katsushika-ku, Tokyo, Japan
email: yamamoto@rs.kagu.tus.ac.jp

Key Words: *Multi-physics CFD, Ice Accretion, Heat Conduction, Jet Engine*

Abstract. *The icing phenomenon is caused by complicated interactions of various physical conditions. Among all of various physical conditions, the impingement distribution, the impingement mass of droplets and the heat transfer from the droplet to the wall are the most influential. However, the temperature of impingement droplets which is used for the heat transfer between the impingement droplet and the wall is generally assumed to be the temperature of the free stream. This assumption might lead to large error of accurate icing simulations in a jet engine, because the gas temperature remarkably changes in passing through a fan rotor and a multi stage compressor. In the present study, we simulate the ice accretion phenomenon with the temperature change of droplets. The obtained results indicate that the maximum difference of the ice volume is 0.714%. Therefore, it is confirmed that the droplet temperature change does not have little effect on the engine icing simulation.*

1 INTRODUCTION

At altitudes in which aircraft operate, clouds contain numerous super-cooled droplets, which impinge and accrete on an aircraft body and an engine components. This phenomenon is referred to as ice accretion. When an ice layer forms on an aircraft wing, the ice adversely affects the aerodynamic performance of the aircraft by increasing drag and reducing lift and may cause a crash. In a jet engine, accreted ice disturbs the inlet flow and can lead to severe performance degradation. Thus, ice accretion phenomenon is a serious problem in aircraft operations, and there have been several instances of an aircraft accident due to the icing. The occurrence areas of the aircraft icing are the main wing, the tail wing, the splitter, the nose cone, the fan blade, the fan exit guide vane (FEGV), and so on. In addition, the latest research indicated that the ice accretion occurred in the engine core components such as a high-pressure compressor [1, 2]. In order to overcome the problems associated with icing, a number of major research institutes around the world, including NASA and ONERA, have been investigating ice accretion phenomena both experimentally and computationally [3-9].

The ice accretion has two types of the ice shape, which are referred to as the rime ice and the glaze ice. The schematic diagram of the difference between both ice shapes is shown in Fig. 1. The rime icing occurs at very low temperature, and super-cooled droplets instantly freeze at the impingement area. On the other hand, the glaze ice is generated at warmer temperature (more than about -10 ˚C) with the runback, which is the phenomenon that the impingement droplet slowly freeze running on the wall surface. Considerably many occurrence factors including the liquid water content (LWC), the velocity and the mass of the impingement droplets, and the ambient temperature are intricately intertwined when the both icing occur. Among all of the occurrence factors, the impingement distribution and the impingement mass of droplets, and the heat transfer from the droplet to the wall are the most influentiall. For the icing simulation, the impingement area of droplets and the wall surface temperature can accurately be estimated. In addition, the impingement mass of the droplet is modeled by the approach of the median volume diameter (MVD), because each droplet diameter in clouds is not clear. However, the temperature of the impingement droplet is generally applied for the temperature of the free stream, which is used for the heat transfer computation from the impingement droplet to the wall [10-12]. This assumption means that the temperature change of the flying droplet is not considered. It is no problem for the icing simulation of the main wing or the tail wing. However, the assumption might be too simplistic for the engine icing simulation, because the flow field in the jet engine is considerably complicated with the shock wave, the high speed rotation, and so on. In addition, the airflow temperature in the jet engine remarkably changes when the droplet pass the fan blade and the multistage compressor passage.

In the present study, we conduct the engine icing simulations by two types of the computational procedure, which are the simulation with and without the temperature change of the flying droplet. Thus, we clarify the effect of the temperature change of the flying droplet on the engine icing simulation. The results obtained from the present study indicate that the existing simulation procedure which does not considered the change of the droplet temperature is no problem for the engine icing simulation.

2 ICING SIMULATION ALGORITHM

In the icing simulation algorithm of the present study, we use the weakly coupling method which includes the grid generation, the flow field computation, the droplet trajectory computation, and the thermodynamics computation. Each computational procedure is described below in details.

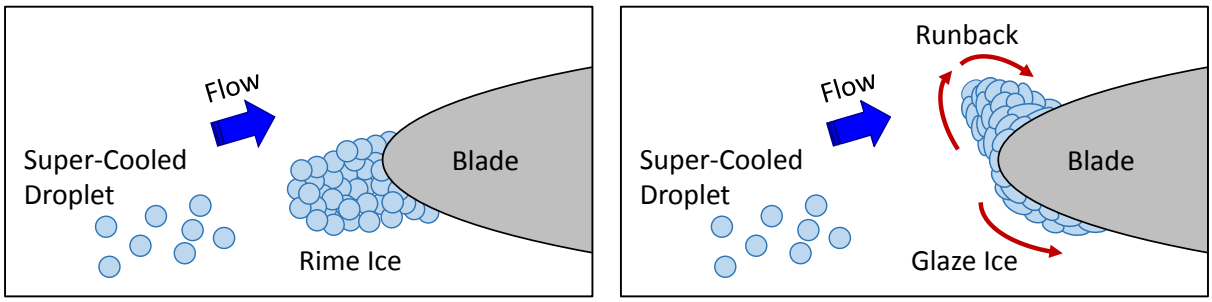

(a) Rime Ice (b) Glaze Ice

Figure 1: Schematic Diagram of Icing Type

2.1 Flow Field

The flow field is assumed to be three-dimensional, compressible, and turbulent. The governing equations are the Favre-averaged continuity, Navier-Stokes, and energy equations. Since a rotational frame of reference is used, the Coriolis force and centrifugal force are added as body forces. The Kato-Launder k-ε turbulence model (Kato and Launder, [13]) is used to estimate turbulence. The governing equations are discretized using the second-order upwind TVD scheme (Yee and Harten, [14]) for the inviscid terms, the second-order central difference scheme for the viscous terms, and the LU-ADI scheme (Fujii and Obayashi, [15]) for the time integration.

2.2 Droplet Trajectory

Droplet trajectory is computed based on a Lagrangian approach in order to obtain the local water distribution on a wall. The computation uses the following assumptions:

(1) A droplets is spherical.
(2) A droplet is are sufficiently small and thus does not break up.
(3) The forces acting on a droplet are drag, centrifugal force, and the Coriolis force.
(4) Droplets do not interact with each other.
(5) Droplets do not affect the flow field (one-way coupling).
(6) The initial droplet velocity is equal to the gas velocity at the release point.

The equation of the droplet motion is

$$\frac{d\vec{U}_d}{dt} = \frac{3}{4} C_D \frac{\rho_f}{\rho_d} \frac{1}{d_d} \vec{U}_r \left|\vec{U}_r\right| - \left\{2\vec{\Omega} \times \vec{U}_d - \vec{\Omega} \times \left(\vec{\Omega} \times \vec{r}_d\right)\right\} \tag{1}$$

where t is the time, U_r is the relative velocity between the gas and the droplet, d_d is the droplet diameter, and ρ_f and ρ_d are the gas and the droplet density. The second term on the right-hand-side represents the centrifugal force and the Coriolis force. The drag coefficient C_D is obtained from Schiller-Naumann equation [16].

$$C_D = \frac{24}{\mathrm{Re}_d}\left(1 + 0.15\,\mathrm{Re}_d{}^{0.687}\right) \tag{2}$$

where Re_d is the realative Reynolds number of a droplet based on the diameter and the relative velocity between the gas and the droplet.

The droplet trajectory is computed in order to obtain the local water distribution, i.e., the impingement distribution of super-cooled droplets on a unit area at each second. The mass flow rate of the inflow droplet in the control volume Q_{in} is as

$$Q_{in} = A_{in} U_{in} LWC \tag{3}$$

where A_{in} is the area of the inlet droplet, U_{in} is the velocity of the inlet droplet, and the LWC is the liquid water content. The number of inflow droplets per second N_{in} is computed as

$$N_{in} = \frac{Q_{in}}{\rho_d V_d} \tag{4}$$

where V_d is the droplet volume. The local ratio of the number of impinging droplets to the total number of droplets P_{im} and the local water distribution β are expressed, respectively, as

$$P_{im} = \frac{N_{im}}{N_{com}} \tag{5}$$

$$\beta = P_{im} \frac{N_{in}}{A_{cell}} \tag{6}$$

where, N_{im} is local number of impingement droplets, N_{com} is total number of computational droplets, A_{cell} is local area of surface cell. The local water distribution is a key parameter in an icing simulation.

The heat conduction of the droplet is computed by the following equation,

$$m_d C_{pd} \frac{dT_d}{dt} = \pi d_d k_d (T_f - T_d) Nu_d \tag{7}$$

where m_d is the mass of the droplet, C_{pd} is the specific heat of the droplet, T_d is the temperature of the droplet, d_d is the diameter of the droplet, k_d is the thermal conductivity of the droplet, and T_f is the temperature of the airflow. In the present study, the evaporation of the flying droplet is not considered since it is too small. The Nusselt number of the droplet Nu_d is obtained from Ranz-Marshall equation [17],

$$Nu_d = 2 + 0.6 + \mathrm{Re}_d^{1/2} \mathrm{Pr}_f^{1/3} \tag{8}$$

where Pr_f is the Prandtl number of the airflow.

2.3 Thermodynamics

The Extended Messinger model which was developed by Orgen and Canibak [11] is used for the thermodynamics computation. This model is based on the Stefan problem, which is a standard method of a phase change problem. The governing equations are expressed as

$$\frac{\partial T_i}{\partial t} = \frac{k_i}{\rho_i C_{pi}} \frac{\partial^2 T_i}{\partial h^2} \tag{9}$$

$$\frac{\partial T_w}{\partial t} = \frac{k_w}{\rho_w C_{pw}} \frac{\partial^2 T_w}{\partial h^2} \tag{10}$$

$$\rho_i \frac{\partial B_i}{\partial t} + \rho_w \frac{\partial B_w}{\partial t} = m_{im} + m_{in} - m_{e,s} \tag{11}$$

$$\rho_i L_F \frac{\partial B_i}{\partial t} = k_i \frac{\partial T_i}{\partial h} - k_w \frac{\partial T_w}{\partial h} \tag{12}$$

where Eqs. (9) and (10) are the energy equations in the ice and the water layer respectively, Eq. (11) is the mass conservation equation and Eq. (12) is the phase change condition at the ice/water interface. In these equations, T_i and T_w are the temperatures of ice and water; B_i and B_w are the thicknesses of ice and water layers; k_i and k_w are the thermal conductivities of ice and water; C_{pi} and C_{pw} are the specific heats of ice and water; m_{im}, m_{in} and $m_{e,s}$ are impinging, runback and evaporating (or sublimating) water mass flow rates for a control volume, respectively; ρ_i and ρ_w are the density of ice and water; L_F denotes the latent heat of

solidification of water. Ice density is assumed to have two different values for rime ice ρ_r and glaze ice ρ_g. The coordinate h is normal to the wall or ice surface.

3 COMPUTATINAL TARGET AND CONDITIONS

3.1 Computational Target and Grids

The icing components in a jet engine are the splitter, the nose cone, the inlet fan, the FEGV, the low pressure compressor, and so on. The computational targets of the present study are the inlet fan and the FEGV since an engine icing easily occurs in these components. Figure 2 shows the computational targets. This rotor-stator cascade is composed of twenty-four fans and sixty FEGVs, though we simulate a fan and two FEGVs for periodicity.

We apply the multi block method and the overset grid method for the grid generation. Figure 3 shows the computational grids, which include the main grids for the passage and the sub-grids for each blade. The total number of grid points is about 2.84 million.

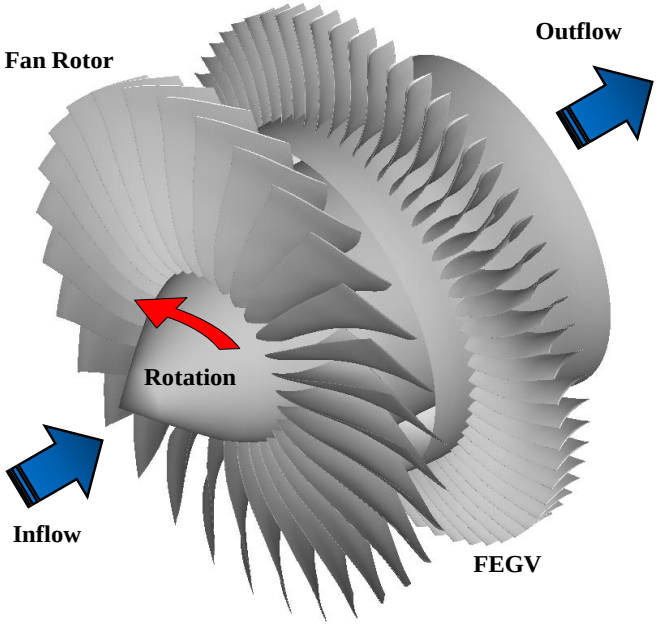

Figure 2: Computational Targets

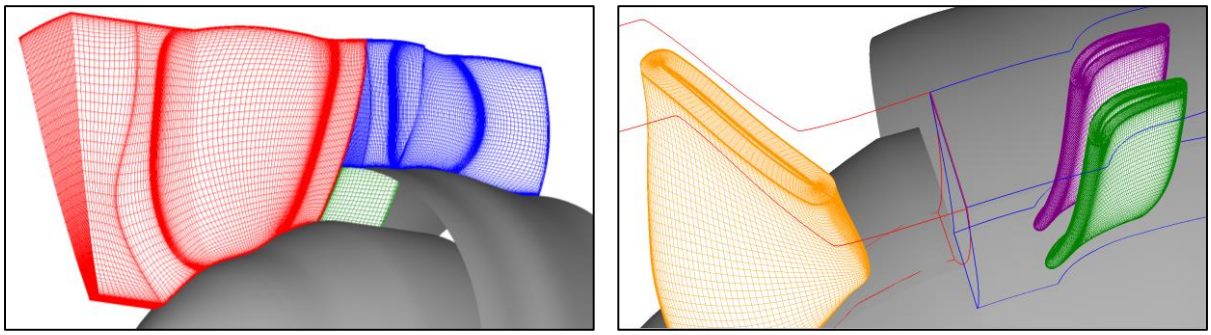

(a) Main Grids (b) Sub-grids

Figure 3: Computational Grids

3.2 Computational Conditions and Boundary Conditions

We simulate two types of the ice shape which are the rime ice and the glaze ice, and two cases of the droplet diameter which are 20 μm and 50 μm MVD. Hence, the total number of the computational cases is four. In addition, each case is respectively computed with the change of the droplet temperature (w/ TC) and without it (w/o TC) in order to clarify the effect of the change of the droplet temperature on the icing simulation. The computational conditions used in the present study are listed in Table 1. The droplet trajectory simulation is conducted for 500,000 droplets that are randomly distributed at the upstream boundary.

The total pressure, total temperature, and flow angle are imposed, and the Mach number is extrapolated at the upstream inflow boundary. The inflow turbulent kinetic energy is assumed based on 0.1% turbulence of the free stream. Adiabatic, no-slip conditions and the wall function are prescribed for the stationary walls and the rotating surfaces. The exit static pressure is specified.

4 RESULTS AND DISCUSSION

4.1 Flow Field

Figure 4 shows the static temperature distribution of the airflow at 90% span in Run 3 (Glaze Ice, MVD 20 μm). In the flow field of the fan, the static temperature rises to higher than 280 K at the stagnation point and falls to about 225 K at the suction side near the leading edge. Therefore, the static temperature remarkably changes around the fan whereas the inlet total temperature is 253.15 K. In addition, the static temperature of the fan wake is higher than others (about 270 K). On the other hand, the flow field of the FEGVs is unsteady due to the fan rotor wake. In the FEGVs which chop the fan wake, the difference of the static temperature between the suction and pressure side is larger, and the static temperature is 275 K at the stagnation point. Thus, in the jet engine, the static temperature of the airflow considerably changes when pass the highly rotating fan.

4.2 Droplet Trajectory and Change of Droplet Temperature

The change of the droplet temperature in Run 3 (Glaze Ice, MVD 20 μm) is shown in Fig. 5. Five droplets set in the inlet boundary of 10%, 50% and 90% span section, respectively. Most droplets impinge on the leading edge of the pressure side at the hub side. On the other hand, at the tip side, a lot of droplets pass the fan and reach the FEGVs. At the whole span section, the droplet temperature increases when the droplet passes the fan. In addition, the temperature of

Table 1: Computational Conditions

		Run 1	Run 2	Run 3	Run 4
Exposure Time	[s]	10.0			
LWC	[g/m^3]	1.0			
Rotating Tip Speed	[m/s]	300			
Inlet Mach Number		0.44			
Inlet Total Pressure	[MPa]	0.1013			
Inlet Total Temperature	[K]	233.15		253.15	
MVD	[μm]	20	50	20	50

the droplet flying at the tip side falls to about 230 K when the droplet passes the shock wave, after that the droplet temperature rises to about 260 K when the droplet reaches the FEGVs. Then, the droplet temperature changes over large temperature range (about 30 K) at the tip side. The droplet passing the fan keeps high temperature and enter the FEGVs. In addition, the temperature of the droplet which goes through the wake of the fan rotor further increases.

Figure 6 shows the temperature change of the droplet in Run 4 (Glaze ice, MVD 50 μm). Although the inlet position of droplets is same as Run 3, the number of droplets which impinge on the fan blade and the end wall is larger than that of Run 3. This occurs by the larger droplet diameter and the stronger inertial force, and these factors also reduce the number of the droplets

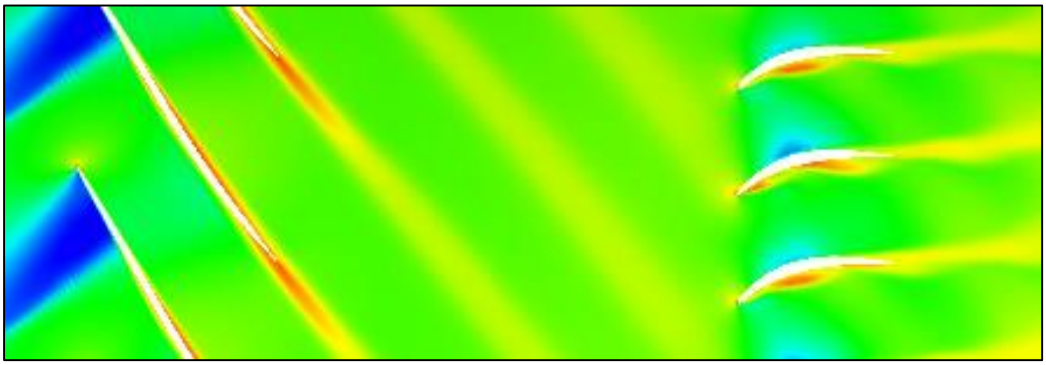

(a) Phase Angle 0 deg.

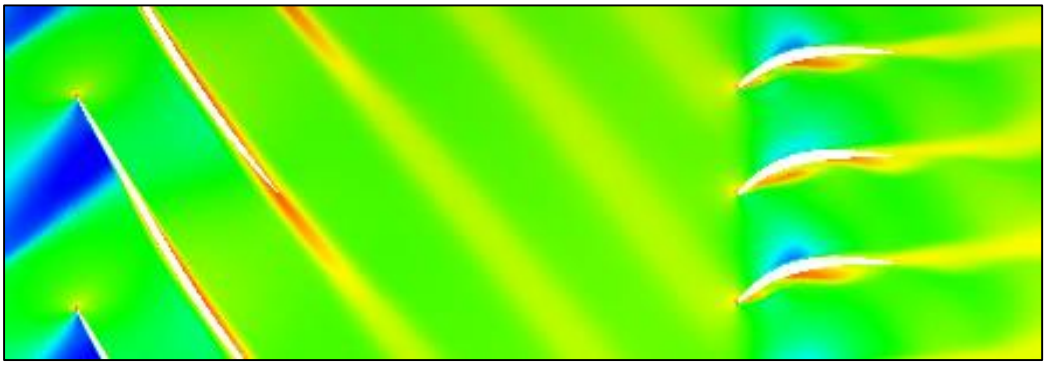

(b) Phase Angle 120 deg.

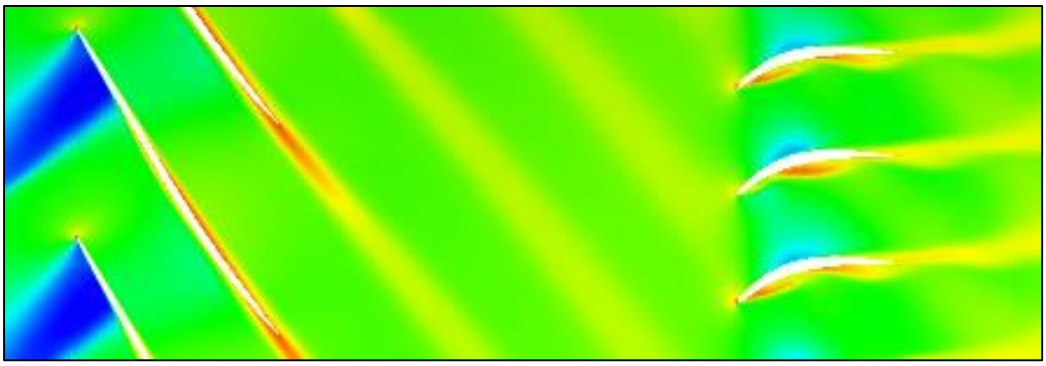

(c) Phase Angle 240 deg.

230 280 [K]

Figure 4: Static Temperature of Airflow at 90% Fan Span (Run 3)

reaching the FEGVs. Furthermore, the temperature change of the droplet passing the fan of Run 4 is lower than that of Run 3, because the droplet of Run 4 has lower heat conduction due to the larger droplet volume. Therefore, the range of the droplet temperature change is about 20 K.

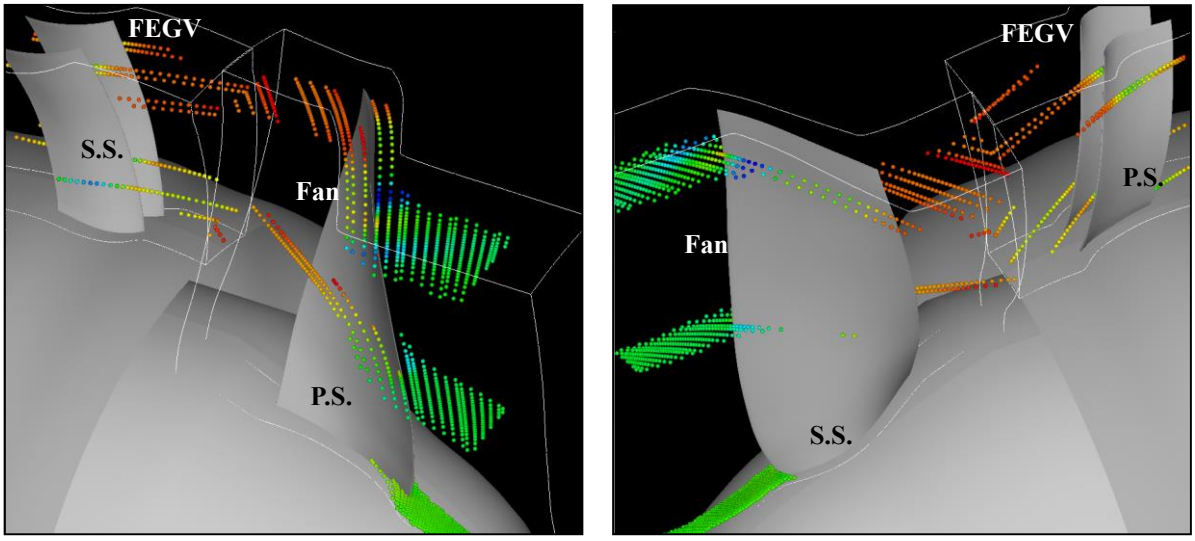

(a) Fan Pressure Side (b) Fan Suction Side

230 260 [K]

Figure 5: Change of Droplet Temperature (Run 3)

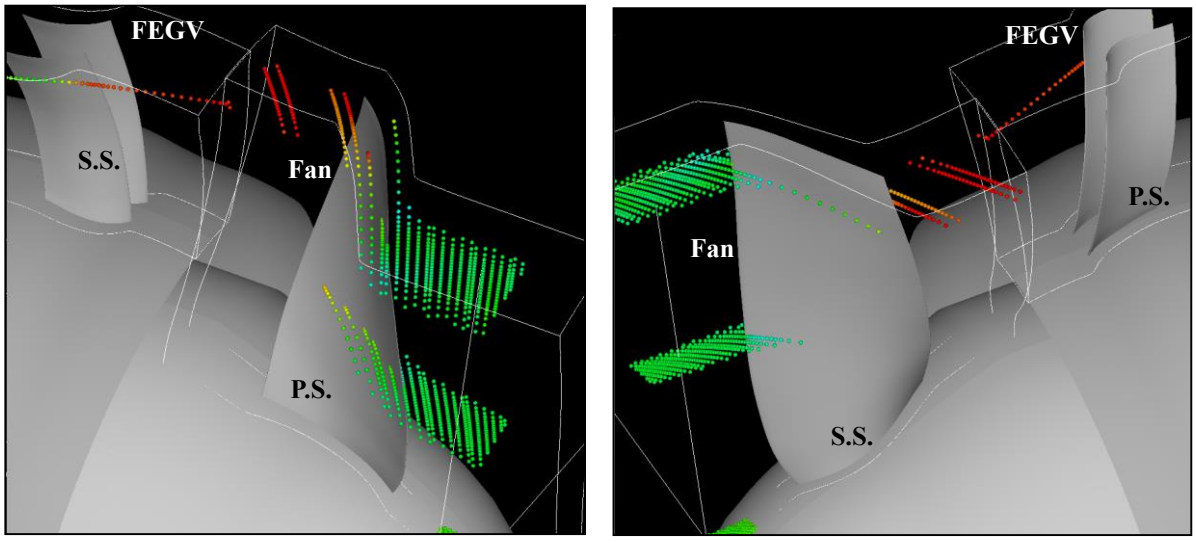

(a) Fan Pressure Side (b) Fan Suction Side

230 260 [K]

Figure 6: Change of Droplet Temperature (Run 4)

Table 2: Difference of Ice Volume between w/ TC and w/o TC

		Run 1	Run 2	Run 3	Run 4
Fan	[%]	0.003	0.012	0.437	0.714
FEGV-1	[%]	0.000	0.000	0.018	0.023
FEGV-2	[%]	0.000	0.000	0.017	0.033

4.3 Effect of Droplet Temperature Change on Icing Simulation

The difference of the ice volume between the simulation with the change of the droplet temperature (w/ TC) and without it (w/o TC) is summarized in Table 2. Among all of simulation

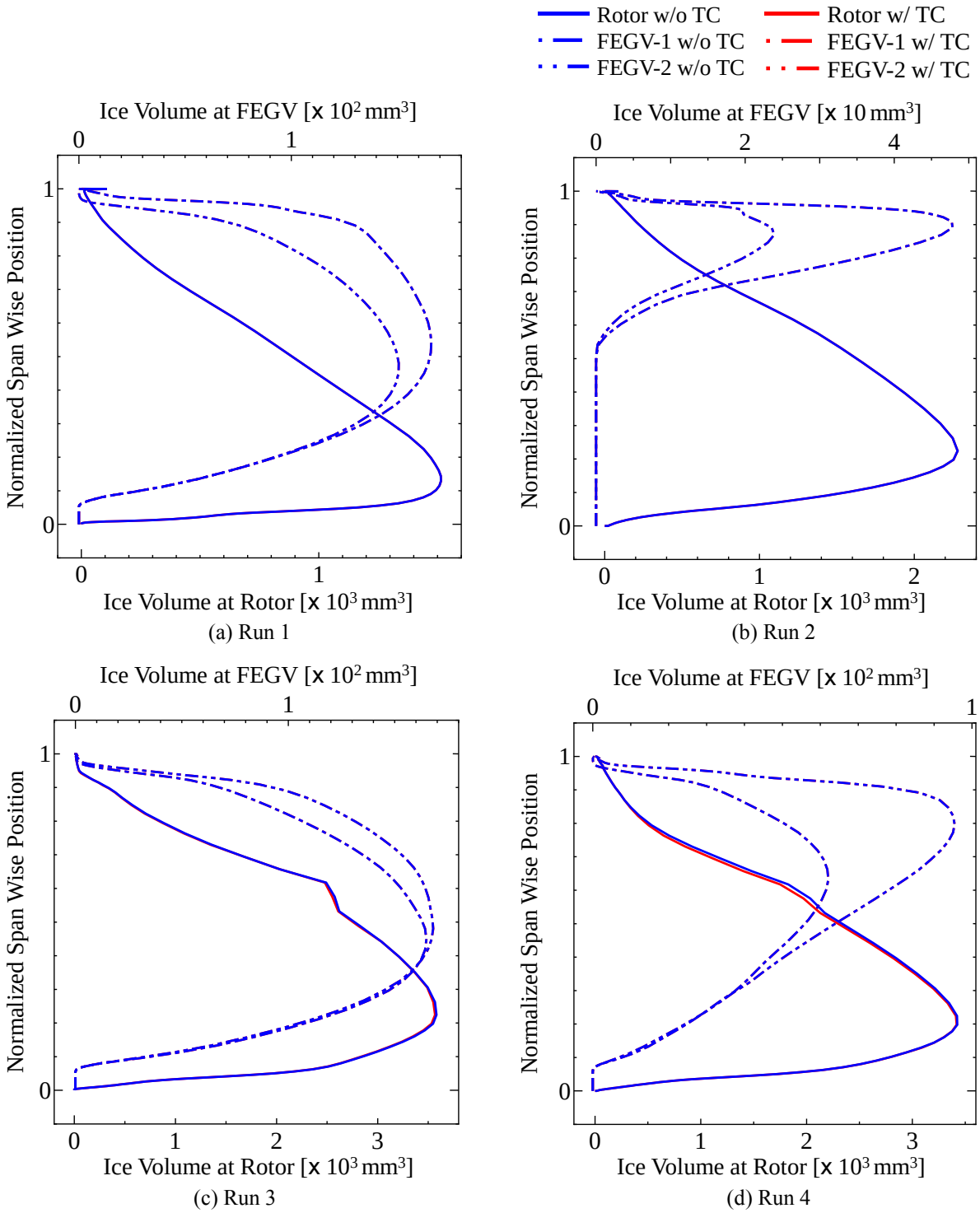

Figure 7: Ice Volume at Whole Cross Span Section

cases, Run 4 is the most influential case for the change of the droplet temperature. Figure 7 shows the ice volume distribution at the whole cross span section. In the most influential component, which is the fan of Run 4, the ice volume of the w/ TC is slightly lower than that of the w/o TC from the thickest ice layer span section to the tip. This would be caused by the runback phenomenon. In the fan icing of Run 4, the ice type is the glaze ice, and the ice volume and the runback mass are the largest. Therefore, the effect of the droplet temperature change appears in the icing simulation which generates a lot of runback mass. However, the maximum difference of the ice volume between w/ TC and w/o TC is only 0.714% in Run 4, and the difference is lower than 1% in all of simulation cases. In addition, the icing area does not change by the effect of the droplet temperature change. Therefore, although the droplet temperature changes by the large range of 30 K due to the passing the fan, this change of the droplet temperature mostly has no influence on the icing simulation. Accordingly, the existing computational procedure which does not consider the temperature change of a flying droplet has no problem for the icing simulation, and it is confirmed that we can set the temperature of an impingement droplet to be the inlet temperature of the free stream.

5 CONCLUSIONS

In the jet engine, we have conducted the icing simulations with the temperature change of the droplet passing the fan in order to clarify the effect of the droplet temperature change on the icing simulation. The obtained results from the present study are as follows:

- In the fan used for the present study, the range of the droplet temperature change is about 30 K when the range of the airflow temperature change is about 50 K.
- In the fan, the difference of the ice volume between the simulation with and without the temperature change of the flying droplet is 0.714%.
- In the fan, the icing area obtained from the simulation with the temperature change of the droplet is same as that from the simulation without the temperature change of the droplet.
- In the icing simulation, the existing computational procedure which applies the temperature of the free stream to the temperature of the impingement droplet has no problem, because the droplet temperature change has little effect on the icing simulation.

REFERENCES

[1] G. Jeanne, J. Mason, W. Strap, and P. Chow, The Ice Particle Threat to Engines in Flight, *Proceeding of 44th AIAA Aerospace Sciences Meeting and Exhibit* (2006).

[2] S. Nilamdeen, and W. G. Habashi, FENSAP-ICE: Modeling of Water Droplets and Ice Crystals, *Proceeding of 1st AIAA Atmospheric and Space Environments Conference* (2009).

[3] B. L. Messinger, Equilibrium Temperature of an Unheated Icing Surface as a Function of Airspeed, *Journal of the Aeronautical Sciences* (1953), Vol. 20, No. 1, pp. 29-42.

[4] W. B. Wright, P. W. Gent and D. Gufford, DRA/NASA/ONERA Collaboration on Icing Research, NASA CR-202349 (1997).

[5] X. Presteau, E. Montreuil, A. Chazottes and X. Vancassel, Experimental and Numerical Study of Scallop Ice on Swept Cylinder, *Proceeding of 1st AIAA Atmospheric and Space Environments Conference* (2009).

[6] J. P. Veres, P. C. E. Jorgenson and W. B. Wright, Modeling the Effects of Ice Accretion on the Low-Pressure Compressor and the Overall Turbofan Engine System Performance, NASA TM-2013-217034 (2011).
[7] J. Hospers and H. Hoeijmakers, Numerical Simulation of SLD Ice Accretions, *SAE Technical Paper* (2011), 2011-38-0071.
[8] C. N. Aliaga, M. S. Aubé, G. S. Baruzzi and W. G. Habashi, FENSAP-ICE-Unsteady: Unified In-Flight Icing Simulation Methodology for Aircraft, Rotorcraft, and Jet Engines, *Journal of Aircraft* (2011), Vol. 48, No. 1, pp. 119-126.
[9] X. Veillard and W. G. Habashi, Icing Simulation in Multistage Jet Engine, *Journal of Propulsion and Power* (2011), Vol. 27, No. 6.
[10] W. B. Wright, User's Manual for LEWICE Version 3.2, NASA CR 214255 (2008).
[11] S. Ozgen and M. Canıbek, Ice accretion simulation on multi-element airfoils using extended Messinger model, *Journal of Heat and Mass Transfer* (2009), Vol. 45, pp. 305-322.
[12] R. Hayashi, K. Kawakami, M. Suzuki, M. Yamamoto, S. Shishido, T. Murooka and H. Miyagaw, Numerical simulation of icing phenomena in fan rotor-stator interaction field, *Proceeding of 11th International Gas Turbine Congress* (2011), pp. 1-5.
[13] M. Kato and B. E. Launder, The modeling of turbulent flow around stationary and vibrating square cylinder, *Proceeding of 8th Symposium on Turbulent Shear Flows* (1993), 10-4-1-10-4-6.
[14] H. C. Yee, Upwind and symmetric Shock-Capturing Schemes, NASA-TM-89464 (1987).
[15] K. Fujii and S. Obayashi, Practical application of improved LU-ADI scheme for the three-dimensional Navier-Stokes computations of transonic viscous flows, *AIAA Paper* (1987), 86-0513.
[16] L. Schiller and A. Naumann, A drag coefficient correlation, Z. Ver. Deutsch (1935), 77, pp. 318-320.
[17] W. E. Ranz and W. R. Marshall, Evaporation from Drops, Chem., Eng. (1952), pp. 141-146.